

# Passive acoustic diagnostics of an atmospheric pressure linear field jet including analysis in the time-frequency domain

N. O'Connor<sup>a)</sup> and S. Daniels

*National Centre for Plasma Science and Technology (NCPST) and School of Electronic Engineering,  
Dublin City University, Collins Avenue, Dublin 9, Ireland*

(Received 11 January 2011; accepted 28 March 2011; published online 14 July 2011)

This study presents the results of passive acoustic diagnostics of an atmospheric pressure linear field jet source operating inflowing helium. Variations of the electrical, optical and acoustic parameters of the source are monitored with respect to changing gas flow rate [0.5–7 liters per minute (lpm)] and applied voltage amplitude (3.5–7 kV). It was found that the jet length and coupled power were maximized when the jet flow was laminar. Flow mode transitions (buoyant, laminar and turbulent) associated with the jet Richardson number could easily be distinguished acoustically through their unique wavelet scalograms. Each scalogram can also be explained through qualitative correlation with the discharge electrical parameters. As the jet became turbulent, low frequency oscillation (c. 180 Hz) bursts were present in the time-frequency trace which were compared to an empirical relation for the Richardson number in the case of flow induced oscillations. It was found that the frequency value correlated well with the frequency of 200 Hz determined from literature. Anomalous sparking events were detected which manifested as almost constant magnitude, broadband acoustic transients in the time-frequency domain. Comparisons between the average acoustic output power and the average dissipated power from the discharge at two different flow rates (4 lpm and 2 lpm) reveal an approximately equal linear trend for a fixed microphone-discharge placement while in the laminar flow regime. Due to the increased turbulence induced noise, however, no such linear correlation could be drawn. Finally, optical emission spectra from the discharge at a point 8 mm downstream of the plume exit were taken and correlations drawn for each flow regime. © 2011 American Institute of Physics. [doi:10.1063/1.3587225]

## I. INTRODUCTION

Owing to their versatility, wealth of applications and reduced costs compared to low pressure plasma systems,<sup>1,2</sup> research and applications of atmospheric pressure nonequilibrium plasma jets have burgeoned in recent decades.<sup>3–11</sup> It has been shown that in the form of linear field, as opposed to cross field, coupling the atmospheric pressure plasma jet plume results in more active chemistry and higher electron temperatures downstream of the plasma generation volume, together with an increased extension of the plume itself.<sup>12</sup> These characteristics of the atmospheric pressure linear field jet (APLFJ) are particularly suitable to biomedical applications and where temperature sensitive material treatments are needed.<sup>1,13</sup>

Contemporary studies of APLFJs have focused on the effects variations in the discharge parameters, particularly the gas flow rate, applied voltage and voltage pulse width, have on the linear field jet plume and its chemistry.<sup>3–11,14–16</sup> Traditional diagnostics of the plasma jets generally incorporate intensified charge-coupled device (ICCD) imaging,<sup>5,9,11,16</sup> current and voltage analysis<sup>6,10,11</sup> and optical emission spectroscopy.<sup>7–10,12</sup>

However, such diagnostics also have certain drawbacks. ICCD imaging is costly and relatively difficult to realize,

while some systems, particularly those in an industrial setting, may not facilitate the installation of current and voltage probes to monitor the discharge electrically. Optical emission spectroscopy is noninvasive and is routinely implemented in both low and atmospheric pressure plasma tools, but spectroscopy systems are relatively expensive and require direct access to the plasma active volume. For these reasons, passive acoustic diagnostics represent a far more favorable alternative to the foregoing diagnostic methodologies as they are low cost, truly noninvasive and can be performed in real time without plasma tool modification or down time.<sup>17</sup>

Although, recently, acoustic diagnostics have been applied to atmospheric pressure plasma systems, the analysis of the plasma acoustic emissions has solely been confined to the frequency domain through the use of the Fourier transform.<sup>18</sup> However, the Fourier transform is not suited to the analysis of highly transient signals,<sup>19</sup> such as those usually found in pulse powered plasma jets.<sup>3–11</sup> A more appropriate tool for inspecting signals which contain transients is the wavelet transform as it offers multi-resolution in the time and frequency domains simultaneously.<sup>19,20</sup> Therefore, in this paper, we analyze and compare the plasma produced acoustic signals in an APLFJ system, with flowing helium, in the time, frequency and time-frequency domains. This work includes the novel implementation of the wavelet transform in the analysis of the plasma jet acoustic emissions.

<sup>a)</sup>Author to whom correspondence should be addressed. Electronic mail: niall.oconnor29@mail.dcu.ie.

## II. THE FOURIER AND WAVELET TRANSFORMS

Conventionally, acoustic signal processing is carried out by means of the Fourier transform. The Fourier transform converts the time domain signal,  $f(t)$ , into the power spectral density, PSD, of the frequency components,  $\omega$ , through convolution with the complex exponential function  $e^{-i\omega t}$  (Ref. 21).

$$F(\omega) = \int_{-\infty}^{\infty} f(t)e^{-i\omega t} dt. \quad (1)$$

However, as stated in the introduction, the Fourier transform is only appropriate for stationary time based signals on which each frequency component,  $\omega$ , is found by integrating over the entire time base of the signal. Therefore, the Fourier transform cannot be used to analyze the spectral components of time based transients in the signal.

The wavelet transform is an efficient method for observing both time based and frequency based information simultaneously from a transient signal.<sup>19</sup> The general definition of the wavelet transform, which may be real or complex, is<sup>19</sup>

$$\begin{aligned} WT_f(\alpha, \tau) &= \int_{-\infty}^{\infty} \frac{1}{\sqrt{a}} f(t) \Psi^* \left( \frac{t-\tau}{a} \right) dt \\ &= \int_{-\infty}^{\infty} f(t) \Psi_{\tau, \alpha}^*(t) dt. \end{aligned} \quad (2)$$

In Eq. (2),  $\psi(t)$  represents the mother wavelet and  $\psi_{\tau, \alpha}(t)$  represents the wavelet which is translated along the time axis by the parameter,  $\tau$  and scaled along the frequency axis by the parameter,  $a$ , while  $*$  represents complex conjugation. Multi-resolution in the time-frequency domain is provided through convolution of the wavelet with the time-based signal using Eq. (2) and scaling in the time and frequency domains using  $\tau$  and  $a$ , respectively. The mother wavelet used in the analysis presented here is the Gabor or complex Morlet wavelet as it provides the optimum multi-resolution of acoustic signals.<sup>20</sup> It is given by

$$\Psi(\alpha, \tau) = \frac{1}{\pi^{\frac{1}{4}}} e^{-\frac{1}{2} \left[ \frac{(t-\tau)^2}{\alpha^2} \right]} e^{i\omega_0 \frac{(t-\tau)}{\alpha}}. \quad (3)$$

The Gabor wavelet is essentially a Gaussian windowed complex sinusoid. It is these features of the wavelet which make it particularly useful in analyzing acoustic signals as they are expected to be almost sinusoidal in shape. In our time-frequency analyses, the wavelet transformations were carried out using 800 frequency scales and 500 time translations on the acoustic signals.

## III. EXPERIMENTAL SET UP AND DIAGNOSTICS

The diagnostic setup is detailed in Fig. 1. As mentioned in Sec. I, linear field driven plasma jets are more efficient at producing active species than their cross field counterparts. Therefore, we have produced a linear field design based on our earlier cross field system.<sup>22</sup> The APLFJ was constructed of a glass tube with inner and outer diameters of 2 mm and 5 mm respectively. Concentric copper foil outer electrodes were placed 10 mm apart and measured 20 mm long for the

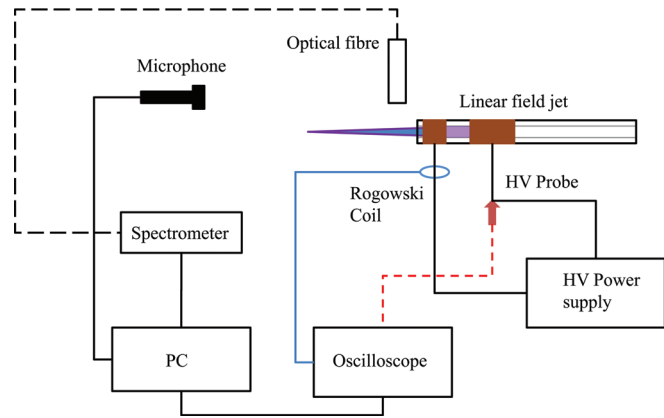


FIG. 1. (Color online) Schematic of the experimental setup. The microphone and optical fiber were placed parallel to the discharge axis setup.

driven electrode and 10 mm long for the grounded electrode. High voltage pulses of 5.4 kV in amplitude and pulse repetition rate of 3.6 kHz were applied to the driven electrode by means of a signal generator, MOSFET, flyback transformer topology.<sup>17,22</sup>

The electrical diagnostics consisted of a high voltage probe on the driven electrode together with a Rogowski coil on the ground path to measure the current through the discharge.

A 200  $\mu\text{m}$ , 1.5 m length optical fiber was mounted perpendicularly to the plume axis at a distance of 5 mm from the termination of the tube. Optical emission spectra were taken at an integration time of 200 ms using a Ocean Optics HR4000 USB spectrometer. A Yoga EM-01 microphone (frequency response 20 Hz –22 kHz) was mounted 100 mm downstream of the plasma plume and off the plume axis to avoid disturbing the gas flow and capture the spherical acoustic pulses generated by the discharge at the tube opening.<sup>23</sup> The acoustic signals were captured continuously at a sampling rate of 96 kS/s and analyzed in the time, frequency and time-frequency domains using a virtual instrument based on the NI Lab-VIEW Advanced Signal Processing Toolkit. The signal processing of the acoustic emissions was performed in quasireal time owing to the computational expense of the wavelet transform algorithm, while the electrical signals were monitored in real time. The results of the wavelet convolution are represented graphically on an intensity map known as the *wavelet scalogram*.

## IV. RESULTS AND DISCUSSION

### A. Acoustic emission scalograms

As shown in Refs. 5, 6, 8, and 15, one of the principal methods to increase the length of the plasma plume is to increase the gas flow rate into the plasma jet device. However, beyond a certain flow rate and hence gas exit velocity, the plasma undergoes a transition from a laminar to turbulent regime, resulting in a shortened, nonuniform plume structure<sup>5,9,15</sup> (see Figs. 3 and 2). To evaluate the effect the changing gas flow rate has on the acoustic signatures the gas flow rate was initially set to 0.5 liters per minute (lpm). The

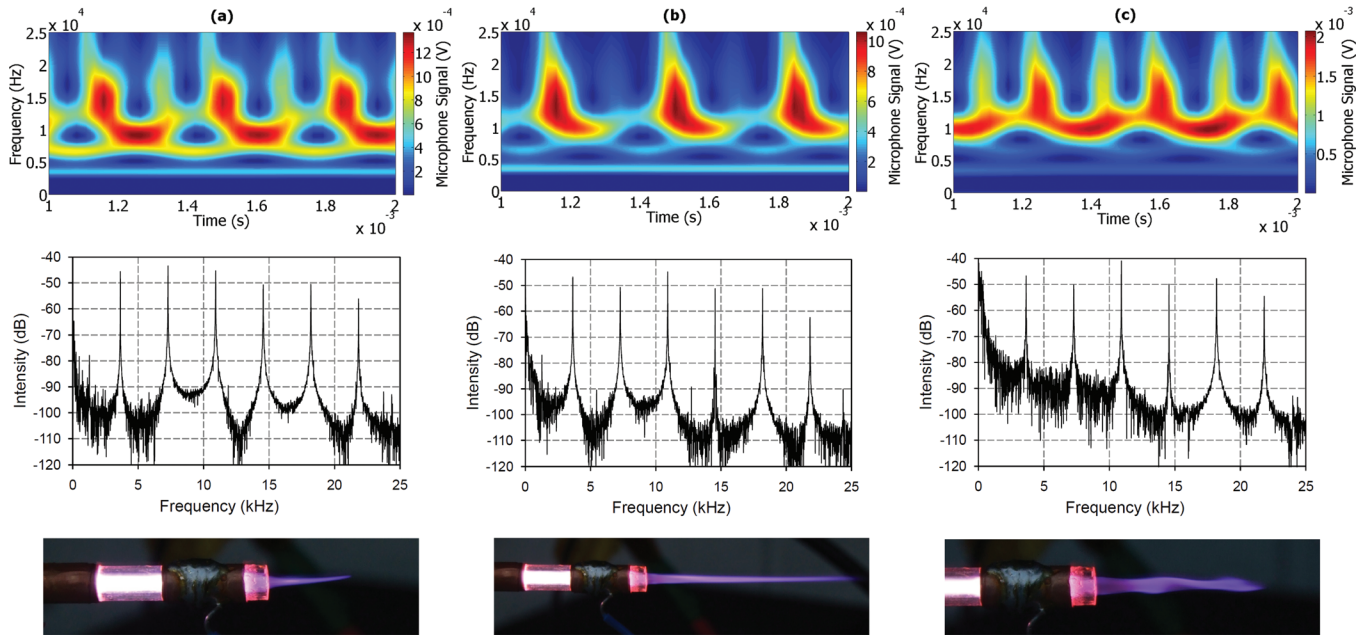


FIG. 2. (Color online) Wavelet scalograms, Fast Fourier Transforms and images of (a) Buoyant plasma plume ( $Q=0.5$  lpm,  $Re=45$ ,  $Ri=1.7 \times 10^{-2}$ ) (b) Laminar and transitional plume ( $Q=3$  lpm,  $Re=271$ ,  $Ri=4.1 \times 10^{-4}$ ) and (c) Turbulent plume ( $Q=7$  lpm,  $Re=633$ ,  $Ri=9.1 \times 10^{-5}$ ).

flow rate was then set to 1 lpm and increased to 7 lpm in 1 lpm steps. The applied voltage amplitude was maintained at approximately 5.4 kV throughout.

Three operating modes, associated with the gas flow rate can be identified in the images of Fig. 2. The flow regimes can be separated into those that are buoyancy dominated [Fig. 2(a)] and the reactive plume follows the helium mole fraction,<sup>5</sup> laminar, momentum dominated flow [Fig. 2(b)], and turbulent flow [Fig. 2(c)].

Inspection of Fig. 2 reveals that, while it is difficult to differentiate between the flow modes of operation of the jet through the Fourier transform (with the exception of an increase in the low frequency noise floor in the turbulent mode), each flow mode produces a unique wavelet scalogram. Although, in the figure, three cycles of the scalogram are produced for clarity, the periodicity of the scalograms

remained over each one second sample interval, with the exception of the turbulent mode [part (c) of Fig. 2], which is discussed later.

There is a qualitative correlation between the scalogram structure and the electrical signals. There were two breakdown events per cycle, one on the voltage rise and another as the voltage pulse changed polarity (see Fig. 4). The amplitude of the second current peak did not change significantly in each mode and was approximately equal to 16 mA. Each successive breakdown is characterized by a strong broadband acoustic emission in the wavelet scalogram which is associated with the almost instantaneous delivery of energy into the discharge followed by the rapid expansion of the gas. In the buoyant mode, the peak current ( $\sim 20$  mA) through the discharge during the first breakdown event is less than that for the laminar-transitional regime ( $\sim 25$  mA) and hence the intensity of the acoustic emission of the second breakdown event signal is reduced in the laminar regime. When the flow becomes turbulent, again the primary current pulse is decreased ( $\sim 19.5$  mA) and the broadband acoustic emission of the second pulse shows a relatively significant increase in the scalogram once more (Note: the scalograms are not phase matched to each other and the most intense broadband acoustic emission of the intensity plots correspond to those of the primary current pulse for each mode).

These flow regimes have been shown to be weakly dependent on the jet flow Reynolds number,  $Re$ , and more strongly dependent on the jet Richardson number,  $Ri$ .<sup>24-27</sup> The respective  $Re$  and  $Ri$  for each of the regimes are included in Fig. 2. The Richardson number may be defined by<sup>28</sup>

$$Ri = \frac{gd(\rho_{\infty} - \rho_0)}{\rho_0 U^2} \quad (4)$$

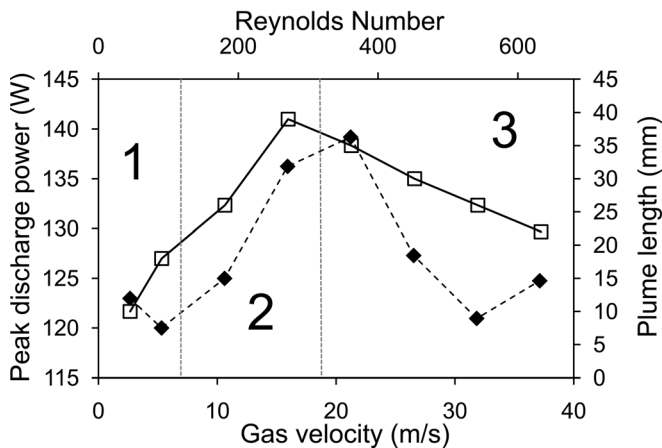


FIG. 3. Variation in the peak dissipated power and plume length extension with respect to gas exit velocity and pipe flow Reynolds number. The figure is divided into (1) Buoyant regime, (2) Laminar-transitional regime and (3) Turbulent regime.

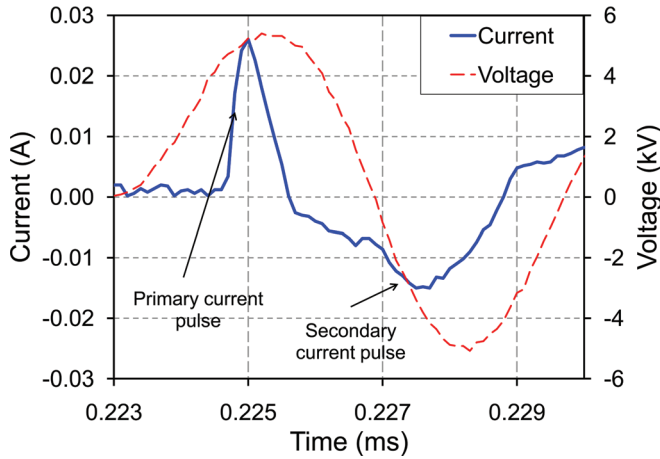


FIG. 4. (Color online) Current voltage characteristics of the APLFJ source. There are two breakdown events - one on the voltage rise (primary current pulse) and one as the voltage changes polarity (secondary current pulse).

where  $\rho_\infty$ ,  $\rho_0$ ,  $d$ ,  $g$ ,  $U$  denote the density of the surrounding air, the density of helium, the hydraulic (inner) diameter of the tube, the acceleration due to gravity and the mean velocity of the gas respectively. The Reynolds number,  $Re$ , is given by<sup>24,28</sup>

$$Re = \frac{Ud}{\nu} \quad (5)$$

where  $\nu$  is the kinematic viscosity of helium,  $1.17 \times 10^{-4} \text{ m}^2\text{s}^{-1}$  (Ref. 28). The gas velocity was determined using  $U = 4Q/\pi d^2$ , where  $Q$  is the volumetric flow rate. The jet Strouhal number, which is related to the frequency of self excited oscillations of the jet in buoyant, mixed density flows, is given by<sup>25</sup>

$$St = \frac{fd}{U}. \quad (6)$$

In Eq. (6),  $f$ , is the frequency of self excited oscillations of the exiting plume. The values for  $Re$  and  $Ri$  for each of the flow modes are included in Fig. 2. It can be seen that the values for the Reynolds number are well below those for pipe flow turbulence to develop ( $\sim 1 \times 10^4$ ).

In Ref. 25, a modified Richardson number,  $Ri_1$ , for helium jets expanding into ambient air, was defined by replacing  $\rho_0$  with  $\rho_\infty$  in the denominator of Eq. (4). An expression was then found in Ref. 25 between  $Ri_1$  and  $St$  given by  $St = 0.8Ri_1^{0.38}$  for  $Ri_1 < 100$ . Further inspection of the wavelet scalograms reveal that as the plume undergoes the transition into the fully turbulent regime low frequency oscillation bursts (c. 180 Hz) are present for time spans of some milliseconds (see Fig. 6). Using the expression in Eq. (6) to determine the predicted frequency of oscillation of the plume from the above relation for  $Ri_1$  gives a value of 200 Hz for an  $Ri_1$  value of  $1.21 \times 10^{-5}$ . This value correlates well with the value observed within the scalogram. Also noteworthy, is that the oscillations were not present over the whole data collection interval and so did not appear as a well defined peak within the Fourier transform.

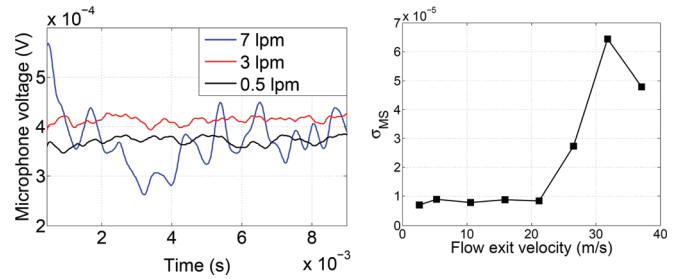


FIG. 5. (Color online) Time frequency analysis of the first harmonic of the acoustic emission from the APLFJ. As the jet undergoes a transition from the laminar to fully turbulent regime the first harmonic amplitude becomes heavily modulated by low frequency disturbances. The standard deviation of the modulation,  $\sigma_{MS}$ , around the mean value of the time based harmonic amplitude is minimized until this point.

As the APLFJ undergoes the transition into the fully turbulent mode it was noticed, through analysis of the time-frequency plots, that the first harmonic of the acoustic signal becomes more heavily modulated by low frequency oscillations. These oscillations are related to the appearance of the low frequency signals described above. A time history of the amplitude of the first harmonic is shown in the left of Fig. 5 for the three modes outlined above. The figure to the right of Fig. 5 shows calculations for the standard deviation of the amplitude of the first harmonic around its mean value,  $\sigma_{MS}$  for all of the flow rates inspected. It is clear from this figure that the turbulent transition, at which the plume length and dissipated power are reduced, can be identified through measurement of  $\sigma_{MS}$  of the first harmonic which shows a steep rise above a gas exit velocity of  $20 \text{ ms}^{-1}$ .

## B. Anomalous spark detection

Anomalous sparking or arcing of the plasma jet can lead to local overheating and substrate or tissue damage.<sup>13,29</sup> A spark event leads to a rapid overheating and expansion of the surrounding gas which can be modeled as a delta like pressure pulse. The Fourier transform of an ideal delta pulse is equal to unity, therefore all frequencies are present at the same magnitude in such signals. Indeed it is this feature of

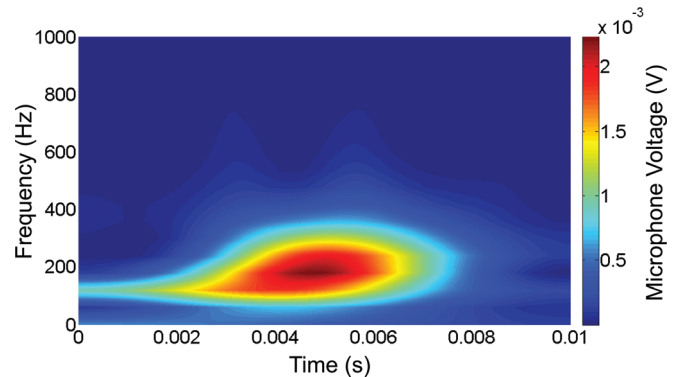


FIG. 6. (Color online) Zoom on the low frequency content of the wavelet scalogram while the flow is turbulent over a period of 10 ms. There are bursts of low frequency oscillations around 180 Hz which persist for 7 ms.



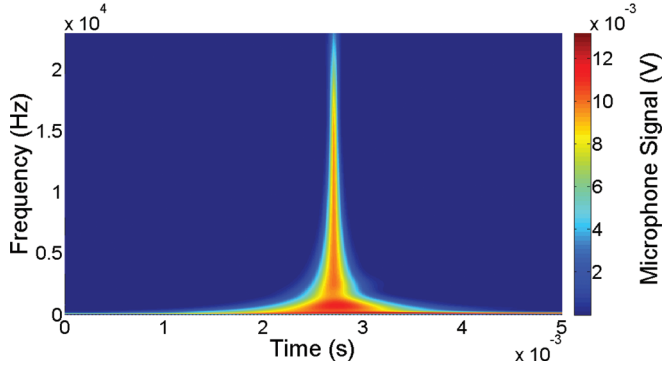


FIG. 7. (Color online) Wavelet scalogram capturing an anomalous sparking event while the plume was in operation.

spark gaps that are invoked in determining the frequency response of acoustic transducers.<sup>23</sup>

In Fig. 7, a discrete acoustic event was captured during the foregoing experiments characterized by an intense signal, the magnitude of which was approximately an order of magnitude greater than previous acoustic signals and whose magnitude was approximately even across the entire frequency content of the scalogram. This was not detected by either the electrical or optical diagnostics. Given the content of the acoustic signal it was most likely the detection of an anomalous spark which may have occurred across the two outer electrodes or within the discharge bulk.

In this Section, the results of measurements of the average acoustic power sensed by the microphone are compared to the average power dissipated in the discharge over a number of cycles,  $n$ . The average acoustic power sensed by the microphone,  $\bar{P}_{acoustic}$ , and the average power dissipated in the discharge,  $\bar{P}_{discharge}$  may be found using Eqs. (7) and (8), respectively.

$$\bar{P}_{acoustic} = \frac{1}{nT} \int_t^{t+nT} \frac{V_A(t)^2}{Z} dt \quad (7)$$

$$\bar{P}_{discharge} = \frac{1}{nT} \int_t^{t+nT} V_D(t) I_D(t) dt. \quad (8)$$

In Eqs. (7) and (8),  $V_A(t)$  and  $V_D(t)$  are the voltages measured with the microphone and high voltage probe respectively,  $Z$  is the impedance of the microphone and sound card (1 k $\Omega$ ),  $I_D(t)$  is the discharge current and  $T$  is the pulse repetition period. The applied voltage to the discharge was increased from 3.5 kV to 7 kV in 0.5 kV steps. Each electrical and acoustic power measurement was performed through averaging

over  $n = 30$  cycles of the electrical and acoustic waveforms. The results of these measurements are presented for two different gas flow rates of 4 lpm (left) and 2 lpm (right) in Fig. 8.

### C. Remote power measurements

It can be seen that for both flow rates there is a very similar linear relationship between the average power dissipated in the discharge and the average acoustic output power. The slopes and intercepts of the linear relationship, together with their respective  $R^2$  values, between the two operating modes are approximately equal. These results imply that for a given distance of the microphone placement from the discharge a noninvasive measurement of the discharge power can be performed through the acoustic sensing while the discharge is operating in the laminar mode with a constant of proportionality approximately equal to  $1/(6.4 \times 10^{-3})$  for the microphone distance in the current experiments. This however was not the case for the turbulent mode as a significant amount of the acoustic power is represented by the pressure oscillations due to the turbulent breakup of the gas jet and hence, the acoustic power measurement is not solely due to the discharge acoustic emissions.

These results are not surprising as they may be interpreted using the theory of Morse and Ingard<sup>30</sup> for acoustic wave generation by a gas discharge. In their work it was proposed that the sound pressure wave,  $p$ , produced by plasma is related to the source term by<sup>30</sup>

$$\frac{1}{c^2} \frac{\partial^2 p}{\partial t^2} - \nabla^2 p = \frac{\gamma - 1}{c^2} e \frac{\partial}{\partial t} (N_e b_e E^2). \quad (9)$$

In Eq. (9),  $c$ , is the wave velocity,  $\gamma$ , the ratio of the specific heats,  $e$ , the electronic charge,  $N_e$ , the electron density,  $b_e$ , the electron mobility and  $E$  the electric field. As the power is coupled into the discharge both the electric field and density increase proportionately and hence, so does the acoustic wave amplitude, therefore we expect the average powers to be proportional to each other as long as the other contributions to the acoustic output from the jet are relatively unimportant. Given that the noise output due to the jet turbulence is of the same order as that from the power coupled into the discharge (c.f. Figures 6 and 2) this contributes to the acoustic power also and hence the method would require further signal processing to remove the jet noise from the acoustic emission. This will be investigated further in our future work.

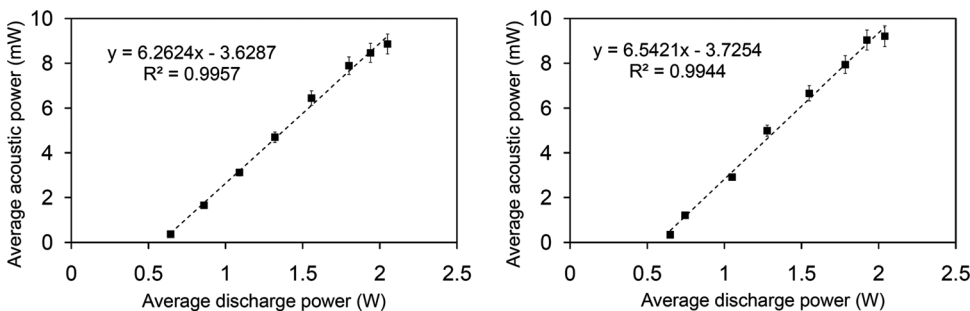


FIG. 8. Remote average discharge power measurement using passive acoustic sensing at gas flow rates of 4 lpm (left) and 2 lpm (right).

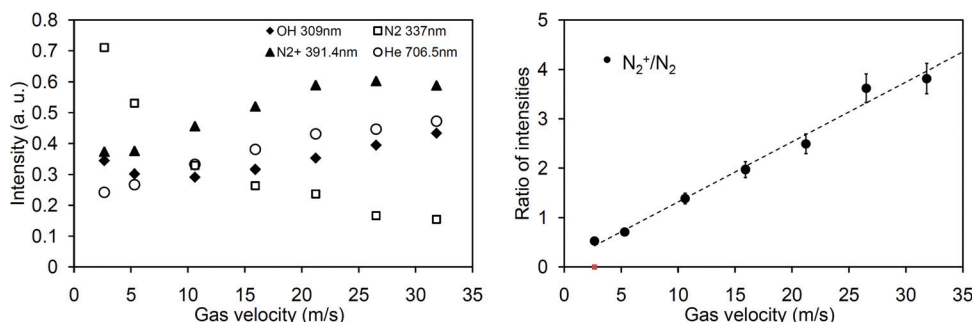


FIG. 9. (Color online) Bulk OES measurements (left) at a point 8 mm downstream of the exit of the glass tube and ratio of the emissions from the molecular nitrogen ion,  $N_2^+$ , at 391.4 nm to the molecular nitrogen emission,  $N_2$ , at 337.1 nm (right).

## D. Optical emission spectroscopy

The analysis of the optical emission spectra consisted of monitoring the  $N_2$  emission at 337.1 nm, the  $N_2^+$  line at 391.4 nm, the 706.5 nm helium emission line and the hydroxyl radical, OH, emission at around 309 nm. The results of the variation of these emission lines with respect to increasing gas velocity are presented to the left of Fig. 9.

The emissions from the 706.5 nm and 391.4 nm lines monotonically increase with gas exit velocity until the flow becomes fully turbulent and a plateau is reached while the 337.1 nm line decreases as the gas velocity increases. More interestingly is the development of the emission from the 309 nm emission line. Initially the intensity drops with increasing gas exit velocity but begins to increase again as the gas velocity increases from  $10 \text{ ms}^{-1}$  to  $15 \text{ ms}^{-1}$ . This could be either attributed to an increase in the electron temperature due to excess helium in the discharge (the first excitation energy of helium  $\sim 20 \text{ eV}$ ) or as a result of water vapor being dislodged from the gas line walls as the gas velocity within the discharge gas feed lines increases.

The increased presence of the emission from the 391.4 nm is due to the Penning ionization reaction ( $\text{He}^* + \text{N}_2 \rightarrow \text{He} + \text{N}_2^+ + e$ )<sup>31</sup> and is indicative of the increase in the metastable helium density as the fraction of air in the gas stream is reduced. This is verified by comparison between the ratio of the emission from the 337 nm line to the 391.4 nm line in the right of Fig. 9 which shows an approximately linear dependence on the gas exit velocity indicating a more efficient metastable production from the surrounding nitrogen impurities.

## V. CONCLUSIONS

We have presented the implementation and analysis of passive acoustic diagnostics in an atmospheric pressure linear field jet system operating inflowing helium. Three flow modes were identified through images taken of the plume while in operation viz. a buoyant mode, a laminar-transitional mode and a turbulent mode. The maximum power coupling into the discharge from the power supply correlated with the maximum extension of the plasma jet plume.

It was found that differentiating the three modes, acoustically, in the frequency domain, through the use of the Fourier transform was relatively difficult. However, analysis of the acoustic emissions in the time-frequency domain through the use of the wavelet transform showed that each flow mode

produced an easily distinguishable, unique scalogram. Each unique scalogram qualitatively represented the electrical characteristics of the distinct break-down events in the corresponding plasma mode.

Further inspection of the low frequency content of the wavelet scalograms revealed that low frequency oscillation bursts of c. 180 Hz frequencies were present over periods of some milliseconds. These oscillations correlated well with the frequency dependence on the flow Richardson number proposed in Ref. 25. Alternatively, we have shown that the transition into the fully turbulent regime of operation of the jet can be identified by taking the standard deviation of the mean of the modulation of the first harmonic of the acoustic signal in the time-frequency domain. It was further revealed that anomalous sparking either between the discharge electrodes or within the plasma bulk could be detected through analysis of the wavelet scalograms also.

Comparisons between the average discharge power and the average acoustic power output from the jet while in the laminar flow regime showed a linear correlation for a set microphone location distance from the discharge exit orifice for two gas flow rates. These results correlate well with the theory of Morse and Ingard for the acoustic pressure wave generated by gas discharge. The reason for no such correlation existing while the jet becomes turbulent has been attributed to the increased flow induced noise contribution by the jet.

Finally, the optical emission spectra shows emission from both the 706.5 nm line and the 391.4 nm line increase monotonically until the jet becomes fully turbulent while the reciprocal happens to the 337.1 nm line. Monitoring of the emission from the hydroxyl radical at 309 nm reveals that the emission goes through an inflection at a gas velocity of  $10 \text{ ms}^{-1}$  which may be attributed to either condensation being freed from the inner walls of the tube or an increase in electron temperature due to the increase in the mole fraction of helium in the discharge.

These results show that passive acoustic diagnostics, together with the novel application of multi-resolution analysis, can be effectively used as a low cost diagnostic in long term, real time monitoring of plasma jet discharges across a variety of power and gas flow ranges.

## ACKNOWLEDGMENTS

The authors acknowledge discussions with Mr. T. Kelly and the technological assistance of Mr. P. Wogan and Mr. H. Leggate. This work is part funded under Enterprise Ireland

Grant CFTD/7/IT/304 and the IMPROVE project funded by the ENIAC Joint Undertaking (project ID: 12005) and IDA Grant No. 133364.

- <sup>1</sup>A. Schutze, J. Jeong, S. Babayan, J. Park, G. Selwyn, and R. Hicks, *IEEE Trans. Plasma Sci.* **26**, 1685 (1998).
- <sup>2</sup>U. Kogelschatz, *Plasma Chem. Plasma Process.* **23**, 1 (2003).
- <sup>3</sup>Q. Li, J. Li, W. Zhu, X. Zhu, and Y. Pu, *Appl. Phys. Lett.* **95**, 141502 (2009).
- <sup>4</sup>X. Lu, Z. Jiang, Q. Xiong, Z. Tang, X. Hu, and Y. Pan, *Appl. Phys. Lett.* **92**, 081502 (2008).
- <sup>5</sup>E. Karakas, M. Koklu, and M. Laroussi, *J. Phys. D* **43**, 155202 (2010).
- <sup>6</sup>Q. Xiong, X. Lu, K. Ostrikov, Z. Xiong, Y. Xian, F. Zhou, C. Zou, J. Hu, W. Gong, and Z. Jiang, *Phys. Plasmas* **16**, 043505 (2009).
- <sup>7</sup>R. Ye and W. Zheng, *Appl. Phys. Lett.* **93**, 071502 (2008).
- <sup>8</sup>W. Zhu, Q. Li, X. Zhu, and Y. Pu, *J. Phys. D* **42**, 202002 (2009).
- <sup>9</sup>N. Mericam-Bourdet, M. Laroussi, A. Begum, and E. Karakas, *J. Phys. D* **42**, 055207 (2009).
- <sup>10</sup>Q. Xiong, X. Lu, Y. Xian, J. Liu, C. Zou, Z. Xiong, W. Gong, K. Chen, X. Pei, F. Zou, J. Hu, Z. Jiang, and Y. Pan, *J. Appl. Phys.* **107**, 073302 (2010).
- <sup>11</sup>A. Shashurin, M. Shneider, A. Dogariu, R. Miles, and M. Keidar, *Appl. Phys. Lett.* **94**, 231504 (2009).
- <sup>12</sup>J. Walsh and M. Kong, *Appl. Phys. Lett.* **93**, 111501 (2009).
- <sup>13</sup>G. Fridman, A. Brooks, M. Balasubramanian, A. Fridman, A. Gutsol, V. Vasilets, H. Ayan, and G. Friedman, *Plasma Processes Polym.* **4**, 370 (2007).
- <sup>14</sup>Y. Xian, X. Lu, Z. Tang, Q. Xiong, W. Gong, D. Liu, Z. Jiang, and Y. Pan, *J. Appl. Phys.* **107**, 063308 (2010).
- <sup>15</sup>Q. Li, X. Zhu, J. Li, and Y. Pu, *J. Appl. Phys.* **107**, 043304 (2010).
- <sup>16</sup>X. Lu, Q. Xiong, Z. Xiong, J. Hu, F. Zhou, W. Gong, Y. Xian, C. Zou, Z. Tang, Z. Jiang, and Y. Pan, *J. Appl. Phys.* **105**, 043304 (2009).
- <sup>17</sup>N. O'Connor and S. Daniels, in *37th EPS Conference on Plasma Physics* (Dublin City University, Dublin, 2010) p. 2.309.
- <sup>18</sup>J. Tynan, V. Law, P. Ward, A. Hynes, J. Cullen, G. Byrne, S. Daniels, and D. Dowling, *Plasma Sources Sci. Technol.* **19**, 015015 (2010).
- <sup>19</sup>C. K. Chui, *An Introduction to Wavelets* (Elsevier Science, San Diego, 1992).
- <sup>20</sup>P. S. Addison, *The Illustrated Wavelet Transform Handbook* (Institute of Physics Publishing, London, 2002).
- <sup>21</sup>C. D. McGillem and G. R. Cooper, *Continuous and Discrete Signal and System Analysis* (Saunders College Publications, Philadelphia, 1991).
- <sup>22</sup>V. Law, V. Milosavljević, N. O'Connor, J. Lalor, and S. Daniels, *Rev. Sci. Instrum.* **79**, 094707 (2008).
- <sup>23</sup>T. Rossing, *Springer Handbook of Acoustics* (Springer Verlag, Berlin, 2007).
- <sup>24</sup>T. Nakamura, *Flow-Induced Vibrations: Classifications and Lessons from Practical Experiences* (Elsevier Science Ltd, 2008).
- <sup>25</sup>B. Cetegen and K. Kasper, *Phys. Fluids* **8**, 2974 (1996).
- <sup>26</sup>R. Satti and A. Agrawal, *Int. J. Heat Fluid Flow* **27**, 336 (2006).
- <sup>27</sup>B. Yildirim and A. Agrawal, *Exp. Fluids* **38**, 161 (2005).
- <sup>28</sup>D. W. Green and R. H. Perry, *Perry's Chemical Engineers' Handbook (8th Edition)* (McGraw Hill, New York, 2008).
- <sup>29</sup>A. Fridman and L. Kennedy, *Plasma Physics and Engineering* (CRC, Boca Raton, 2004).
- <sup>30</sup>P. Morse and K. Ingard, *Theoretical Acoustics* (Princeton University Press, Princeton, 1986).
- <sup>31</sup>N. Bibinov, A. Fateev, and K. Wiesemann, *J. Phys. D* **34**, 1819 (2001).